

# Study of Three-Nucleon Dynamics in the dp breakup collisions using the WASA detector

P. Adlarson,<sup>1</sup> W. Augustyniak,<sup>2</sup> W. Bardan,<sup>3</sup> M. Bashkanov,<sup>4</sup> F.S. Bergmann,<sup>5</sup> M. Berłowski,<sup>6</sup> A. Bondar,<sup>7,8</sup> M. Büscher,<sup>9,10</sup> H. Calén,<sup>1</sup> I. Ciepał,<sup>11</sup> H. Clement,<sup>12,13</sup> E. Czerwiński,<sup>3</sup> K. Demmich,<sup>5</sup> R. Engels,<sup>14</sup> A. Erven,<sup>15</sup> W. Erven,<sup>15</sup> W. Eyrich,<sup>16</sup> P. Fedorets,<sup>14,17</sup> K. Föhl,<sup>18</sup> K. Fransson,<sup>1</sup> F. Goldenbaum,<sup>14</sup> A. Goswami,<sup>14,19</sup> K. Grigoryev,<sup>14,20</sup> L. Heijkenkjöld,<sup>1,\*</sup> V. Hejny,<sup>14</sup> N. Hüskens,<sup>5</sup> L. Jarczyk,<sup>3</sup> T. Johansson,<sup>1</sup> B. Kamys,<sup>3</sup> G. Kemmerling,<sup>15,†</sup> A. Khoukaz,<sup>5</sup> A. Khreptak,<sup>3</sup> D.A. Kirillov,<sup>21</sup> S. Kistryn,<sup>3</sup> H. Kleines,<sup>15,†</sup> B. Klos,<sup>22</sup> W. Krzemień,<sup>6</sup> P. Kulessa,<sup>11</sup> A. Kupś,<sup>1,6</sup> K. Lalwani,<sup>23</sup> D. Lersch,<sup>14,‡</sup> B. Lorentz,<sup>14</sup> A. Magiera,<sup>3</sup> R. Maier,<sup>14,24</sup> P. Marciniowski,<sup>1</sup> B. Mariański,<sup>2</sup> H.–P. Morsch,<sup>2</sup> P. Moskal,<sup>3</sup> W. Parol,<sup>11</sup> E. Perez del Rio,<sup>12,13,§</sup> N.M. Piskunov,<sup>21</sup> D. Prasuhn,<sup>14</sup> D. Pszczel,<sup>1,6</sup> K. Pysz,<sup>11</sup> J. Ritman,<sup>14,24,25</sup> A. Roy,<sup>19</sup> O. Rundel,<sup>3</sup> S. Sawant,<sup>26</sup> S. Schadmand,<sup>14</sup> T. Sefzick,<sup>14</sup> V. Serdyuk,<sup>14</sup> B. Shwartz,<sup>7,8</sup> T. Skorodko,<sup>12,13,27</sup> M. Skurzok,<sup>3,§</sup> J. Smyrski,<sup>3</sup> V. Sopov,<sup>17</sup> R. Stassen,<sup>14</sup> J. Stepaniak,<sup>6</sup> E. Stephan,<sup>22</sup> G. Sterzenbach,<sup>14</sup> H. Stockhorst,<sup>14</sup> H. Ströher,<sup>14,24</sup> A. Szczurek,<sup>11</sup> A. Trzciński,<sup>2,¶</sup> M. Wolke,<sup>1</sup> A. Wrońska,<sup>3</sup> P. Wüstner,<sup>15</sup> A. Yamamoto,<sup>28</sup> J. Zabierowski,<sup>29</sup> M.J. Zieliński,<sup>3</sup> J. Złomańczuk,<sup>1</sup> P. Żuprański,<sup>2</sup> and M. Żurek<sup>14,\*\*</sup>  
(WASA-at-COSY Collaboration)

A. Deltuva,<sup>30</sup> J. Golak,<sup>31</sup> A. Kozela,<sup>32</sup> R. Skibiński,<sup>31</sup> I. Skwira-Chalot,<sup>33</sup> and H. Witała<sup>31</sup>

- <sup>1</sup>Division of Nuclear Physics, Department of Physics and Astronomy, Uppsala University, Box 516, 75120 Uppsala, Sweden  
<sup>2</sup>Nuclear Physics Division, National Centre for Nuclear Research, ul. Hoza 69, 00-681, Warsaw, Poland  
<sup>3</sup>Institute of Physics, Jagiellonian University, prof. Stanisława Łojasiewicza 11, 30-348 Kraków, Poland  
<sup>4</sup>School of Physics and Astronomy, The University of Edinburgh, James Clerk Maxwell Building, Peter Guthrie Tait Road, Edinburgh EH9 3FD, Great Britain  
<sup>5</sup>Institut für Kernphysik, Westfälische Wilhelms-Universität Münster, Wilhelm-Klemm-Str. 9, 48149 Münster, Germany  
<sup>6</sup>High Energy Physics Division, National Centre for Nuclear Research, ul. Hoza 69, 00-681, Warsaw, Poland  
<sup>7</sup>Budker Institute of Nuclear Physics of SB RAS, 11 Acad. Lavrentieva Pr., Novosibirsk, 630090 Russia  
<sup>8</sup>Novosibirsk State University, 2 Pirogova Str., Novosibirsk, 630090 Russia  
<sup>9</sup>Peter Grünberg Institut, PGI-6 Elektronische Eigenschaften, Forschungszentrum Jülich, 52425 Jülich, Germany  
<sup>10</sup>Institut für Laser- und Plasmaphysik, Heinrich Heine Universität Düsseldorf, Universitätsstr. 1, 40225 Dsseldorf, Germany  
<sup>11</sup>The Henryk Niewodniczański Institute of Nuclear Physics, Polish Academy of Sciences, ul. Radzikowskiego 152, 31-342 Kraków, Poland  
<sup>12</sup>Physikalisches Institut, Eberhard Karls Universität Tübingen, Auf der Morgenstelle 14, 72076 Tübingen, Germany  
<sup>13</sup>Kepler Center for Astro and Particle Physics, Physikalisches Institut der Universität Tübingen, Auf der Morgenstelle 14, 72076 Tübingen, Germany  
<sup>14</sup>Institut für Kernphysik, Forschungszentrum Jülich, 52425 Jülich, Germany  
<sup>15</sup>Zentralinstitut für Engineering, Elektronik und Analytik, Forschungszentrum Jülich, 52425 Jülich, Germany  
<sup>16</sup>Physikalisches Institut, Friedrich-Alexander Universität Erlangen-Nürnberg, Erwin-Rommel-Str. 1, 91058 Erlangen, Germany  
<sup>17</sup>Institute for Theoretical and Experimental Physics named by A.I. Alikhanov of National Research Centre “Kurchatov Institute”, 25 Bolshaya Cheremushkinskaya Str., Moscow, 117218 Russia  
<sup>18</sup>II. Physikalisches Institut, Justus-Liebig-Universität Gießen, Heinrich-Buff-Ring 16, 35392 Giessen, Germany  
<sup>19</sup>Discipline of Physics, Indian Institute of Technology Indore, Khandwa Road, Indore, Madhya Pradesh 453 552, India  
<sup>20</sup>High Energy Physics Division, Petersburg Nuclear Physics Institute named by B.P. Konstantinov of National Research Centre “Kurchatov Institute”, 1 mkr. Orlova roshcha, Leningradskaya Oblast, Gatchina, 188300 Russia  
<sup>21</sup>Veksler and Baldin Laboratory of High Energiy Physics, Joint Institute for Nuclear Physics, 6 Joliot-Curie, Dubna, 141980 Russia  
<sup>22</sup>August Chelkowski Institute of Physics, University of Silesia, ul. 75 Pułku Piechoty 1, 41-500 Chorzów, Poland  
<sup>23</sup>Department of Physics, Malaviya National Institute of Technology Jaipur, JLN Marg, Jaipur, Rajasthan 302 017, India  
<sup>24</sup>JARA-FAME, Jülich Aachen Research Alliance, Forschungszentrum Jülich, 52425 Jülich, and RWTH Aachen, 52056 Aachen, Germany  
<sup>25</sup>Institut für Experimentalphysik I, Ruhr-Universität Bochum, Universitätsstr. 150, 44780 Bochum, Germany  
<sup>26</sup>Department of Physics, Indian Institute of Technology Bombay, Powai, Mumbai, Maharashtra 400 076, India  
<sup>27</sup>Department of Physics, Tomsk State University, 36 Lenin Ave., Tomsk, 634050 Russia  
<sup>28</sup>High Energy Accelerator Research Organisation KEK, Tsukuba, Ibaraki 305-0801, Japan  
<sup>29</sup>Astrophysics Division, National Centre for Nuclear Research, Box 447, 90-950 Łódź, Poland  
<sup>30</sup>Institute of Theoretical Physics and Astronomy, Vilnius University, Saultekio al. 3, LT-10257 Vilnius, Lithuania  
<sup>31</sup>Institute of Physics, Jagiellonian University, prof. Stanisława Łojasiewicza 11, 30-348 Kraków, Poland  
<sup>32</sup>The Henryk Niewodniczański Institute of Nuclear Physics, Polish Academy of Sciences, Radzikowskiego 152, 31-342 Kraków, Poland

<sup>33</sup>*Faculty of Physics, University of Warsaw, Warsaw, Poland*  
(Dated: January 27, 2022)

Differential cross section for the  $^1\text{H}(d, pp)n$  breakup reaction at deuteron beam energy of 340 MeV has been measured with the use of WASA detector at COSY-Jülich. The set of proton-proton coincidences registered at Forward Detector has been analysed on dense grid of kinematic variables, giving in total around 5600 data points. The cross section data are compared to theoretical predictions based on the state-of-the-art nucleon-nucleon potentials, combined with three-nucleon force, Coulomb interaction or carried out in a relativistic regime.

## I. INTRODUCTION

Properties of few-nucleon systems at medium energies are determined to large extent by pairwise nucleon-nucleon (NN) interaction, which are a dominant component of the nuclear potential. NN interactions are described either by the realistic potentials [1–3] or the potentials derived from Chiral Effective Field Theory (ChEFT) [4–6], achieving in both cases a precise description of observables for two-nucleon systems. The deficiencies in description of systems consisting of three and more nucleons are usually attributed to additional part of dynamics, beyond the NN interactions. The so-called three-nucleon force (3NF) is interpreted as a consequence of internal degrees of freedom of interacting nucleons. The 3NF arises in the meson-exchange picture as an intermediate excitation of a nucleon to a  $\Delta$  isobar. State-of-the-art models of 3NF's, like TM99 [7], Urbana IX [8], or Illinois [9], combined with the realistic nucleon-nucleon (2N) potentials, constitute the basis for calculations of binding energies and scattering observables. Chiral Effective Field Theory provides a systematic construction of nuclear forces in a fully consistent way: the 3N forces appear naturally at a certain order [6, 10]. The theoretical calculations including semi-phenomenological 3NF or 3NF stemming from ChEFT, reproduce with high accuracy binding energies of light nuclei [11–14]. They provide also significantly improved description of differential cross section for elastic nucleon-deuteron scattering as compared to the calculations based on NN interactions only [15–17]. Improvement in the sector of polarization observables is not so clear, see discussion in Refs.[18, 19], but this issue will not be further considered in this paper which is focused on the cross section. However, even in the sector of the differential cross section, at

beam energies above 100 MeV/nucleon certain discrepancies between the scattering data and calculations persist. Neither Coulomb interactions between protons [20] nor relativistic effects [21] are able to explain that observation, since their impact, except for very forward angles, where the Coulomb interaction plays a decisive role, is very small in this energy range.

Studies of the  $^1\text{H}(d, pp)n$  and  $^2\text{H}(p, pp)n$  breakup reactions make important contribution to investigations of the 3NF effects. The advantage relies on kinematic richness of the three-body final state. There are experimental evidences of significant 3NF contributions to the differential cross section for the breakup reaction, starting at relatively low beam energy of 65 MeV/nucleon [19, 22]. In contrast to the elastic scattering, Coulomb interaction is a very important component of the breakup reaction dynamics. The Coulomb interaction between protons modifies the cross section data over significant part of the phase space, in particular at forward laboratory angles of the  $^1\text{H}(d, pp)n$  reaction [23, 24]. The Coulomb effects are dominating in the region of configurations characterised with low relative momentum of the proton pair, the so called proton-proton Final State Interaction (FSI) configurations. At present, the Coulomb interaction and 3N forces are both included into theoretical calculations and their interplay can be studied [25–27].

At energies above 140 MeV/nucleon, practically there are no data for the breakup reaction. The only exception, measurement at 190 MeV [28, 29], provided hints of deficiencies in description of the cross section for the deuteron breakup reaction, even when 3NF is included. The problem can be interpreted either as confirmation of mentioned earlier problems observed in elastic scattering cross section, or as a consequence of relativistic effects. In contrary to elastic scattering, the relativistic calculations of the differential cross section for breakup reaction lead to different results than the non-relativistic ones [30]. Due to the significant predicted 3NF and relativistic effects in the energy region between 150 and 200 MeV/nucleon [30, 31], the question arises about their interplay. So far, there has been no calculation with full relativistic treatment of NN and 3NF interactions. Under such circumstances one has to rely on systematic (in beam energy) studies over large phase space regions, with the aim to single out both contributions on the basis of their different kinematic dependencies.

An experiment to investigate the  $^1\text{H}(d, pp)n$  breakup reaction using a deuteron beam of 300, 340, 380 and 400 MeV (150, 170, 190, 200 MeV/nucleon) and the

---

\* present address: Institut für Kernphysik, Johannes Gutenberg Universität Mainz, Johann-Joachim-Becher Weg 45, 55128 Mainz, Germany

† present address: Jülich Centre for Neutron Science JCNS, Forschungszentrum Jülich, 52425 Jülich, Germany

‡ present address: Department of Physics, Florida State University, 77 Chieftan Way, Tallahassee, FL 32306-4350, USA

§ present address: INFN, Laboratori Nazionali di Frascati, Via E. Fermi, 40, 00044 Frascati (Roma), Italy

¶ deceased

\*\* present address: Nuclear Science Division, Lawrence Berkeley Laboratory, One Cyclotron Road, Berkeley, CA 94720-8153, United States

WASA (Wide Angle Shower Apparatus) detector, has been performed at the Cooler Synchrotron COSY-Jülich. Due to almost  $4\pi$  acceptance and moderate detection threshold of the WASA system, differential cross section data have been collected in a large part of the breakup reaction phase space. As a first step the data collected at the beam energy of 170 MeV/nucleon have been analysed, with a focus on the proton-proton coincidences registered in the Forward Detector.

## II. EXPERIMENT AND DATA ANALYSIS

### A. Setup and measurement procedure

The WASA detector [32–34], covering almost full solid angle, consists of four main components: Central Detector (CD), Forward Detector (FD), Pellet Target Device and Scattering Chamber (see Fig. 1).

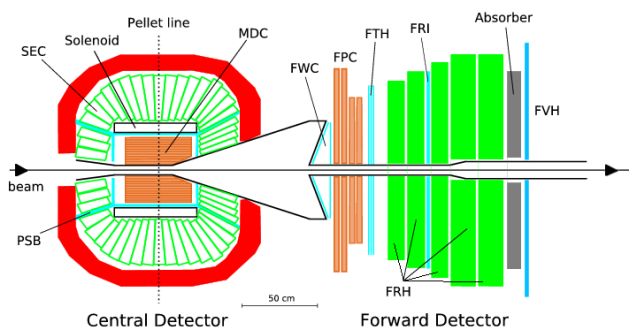


FIG. 1. (Color online) Schematic view of the detection system.

COSY has functionality to group up different machine settings within a “supercycle” which allows to change the beam energy in discrete steps from cycle to cycle [35]. This feature is very useful for the purpose of comparing the cross section at various beam energies. During the  $^1\text{H}(d, pp)n$  measurement energies 170, 190 and 200 MeV/nucleon of the deuteron beam were changed in supercycle mode of time length 30 s (measurement at 150 MeV/nucleon was performed separately), using a barrier bucket cavity. A barrier bucket cavity can be used to compensate the beam energy loss induced by an internal pellet target [36].

The pellet target is a unique development for the CELSIUS/WASA experiment. The target provides a narrow stream of very small frozen hydrogen or deuterium droplets with diameters down to  $25\,\mu\text{m}$ , called pellets. Some of the parameters of the pellet target are listed in Table I.

FD covers the region of the polar angles from  $2.5^\circ$  to  $18^\circ$ . It consists of a set of detectors for the identification of charged hadrons and track reconstruction: Forward Window Counter (FWC), Forward Proportional Chamber (FPC), Forward Trigger Hodoscope (FTH), Forward

TABLE I. Performance of the pellet target system [32]

pellet diameter ( $\mu\text{m}$ )	25-35
pellet frequency (kHz)	5-12
pellet-pellet distance (mm)	9-20
beam diameter (mm)	2-4
effective target area density (atoms/ $\text{cm}^2$ )	$>10^{15}$

Range Hodoscope (FRH) and Forward Veto Hodoscope (FVH). Between the second and third layers of FRH there are two layers of Forward Range Interleaving Hodoscope (FRI). FPC is used for precise determination of particle emission angles. The FD plastic scintillators are used for particle identification and particle energy measurement. They all provide information for the first level trigger logic. Some features of the FD are given in Table II. CD was used in the experiment described here, but the present data analysis do not include particles registered in that part. For description of the CD see Refs. [32, 33].

TABLE II. Basic information on the FD

number of scintillator elements	340
scattering angle coverage	$2.5^\circ$ - $18^\circ$
scattering angle resolution	$0.2^\circ$
amount of sensitive material	$50\,\text{g}/\text{cm}^2$
- in radiation length	$\approx 1\,\text{g}/\text{cm}^2$
- in nuclear interaction length	$\approx 0.6\,\text{g}/\text{cm}^2$
maximum kinetic energy ( $T_{\text{stop}}$ )	
for stopping $\pi^\pm/p/d/^4\text{He}$	170/340/400/900 MeV
time resolution	$\leq 3\,\text{ns}$
energy resolution for	
stopped particles	1.5%-3%
particles with $T_{\text{stop}} < T < 2T_{\text{stop}}$	3%-8%
particle identification	$\Delta E$ -E, $\Delta E$ - $\Delta E$

During data taking for the dp breakup experiment described here there were a few trigger types in use. Trigger named No. 7 was the basic trigger for registering events in FD detector. It required at least one track with correct matching of clusters in FWC, FTH and FRH. It was later used in the analysis of single tracks of deuterons from the elastic scattering and of proton-proton coincidences from the breakup reaction. Trigger named No. 2 was much less restrictive: one hit above threshold was required. Due to high rate of events accepted by this trigger prescaling by a factor 10 was necessary. The comparison of results obtained with triggers 2 and 7 is important for controlling possible bias imposed by trigger conditions.

## B. Data analysis

The data analysis presented in this work is focused on the proton-proton coincidences from the  $^1\text{H}(d, pp)n$  breakup reaction at 170 MeV/nucleon registered in the FD. The aim of our study is the determination of the differential cross section on a dense angular grid of kinematical configurations defined by the emission angles of the two outgoing protons: two polar angles  $\theta_1$  and  $\theta_2$  (in the range between  $5^\circ$  and  $15^\circ$ ) and the relative azimuthal angle  $\varphi_{12}$  (in the wide range between  $20^\circ$  and  $180^\circ$ ).

### 1. Event selection and particle identification

The first step of data analysis is the selection of events of interest, *i.e.* two protons from the breakup process and deuterons from elastic scattering channel registered in the FD. The particle identification is based on the  $\Delta E$ - $E_R$  technique, where  $E_R$  is remaining energy deposit in the layer where particle is stopped (see example in Fig. 2, top panel). In the whole range of energies, a clear separation between loci of protons and deuterons is observed. The analogous spectra are built for data generated in Monte Carlo simulation, separately for elastic scattering and breakup reaction, see example of the deuteron distribution in Fig. 2, bottom panel. The simulation is used to verify cuts set on the data. The only difference between experimental data and simulation spectra is due to particles punching-through the 3rd layer of FRH and stopped in the inactive layer behind it (not included in the simulation). For those events total energy is reconstructed on the basis of energy loss in the 2nd layer.

### 2. Energy calibration

Energy calibration of FD is based on measurements of dp elastic scattering at energies corresponding to minimum ionization with non-uniformity and nonlinearity corrections, as described in detail in Ref. [37]. Since the FRI detector was not used in a number of previous runs, its calibration is not included in the main calibration procedure and is known with lower accuracy. The appropriate corrections have been applied, but in case of protons stopped in FRI (protons with initial energy of about 200 MeV) the energy resolution is diminished. In order to avoid the systematic error related to this effect, the affected energy region has been rejected from the cross section analysis.

### 3. Analysis of the breakup reaction

The missing mass spectrum is a tool to control the proton energy calibration and the procedure of selection of proton-proton coincidences. The missing mass of the

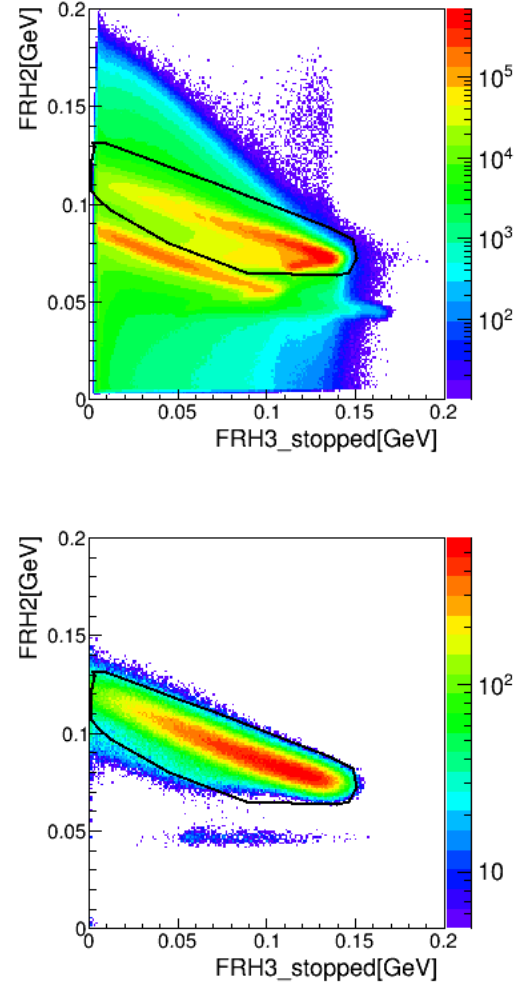


FIG. 2. Particle identification spectra for particles stopped in the 3rd layer of FRH. The “banana-shaped” gate represents the cut applied to select deuterons, the same for experimental data (top panel) and Monte Carlo simulation (bottom panel).

neutron is calculated according to the formula (in which  $c = 1$ ):

$$MM = \sqrt{(E_{in} - E_{p1} - E_{p2})^2 - (\vec{P}_{in} - \vec{P}_{p1} - \vec{P}_{p2})^2}, \quad (1)$$

where  $E_{in}$  and  $\vec{P}_{in}$  are the sum of energy and momenta of the incident deuteron and target proton and  $E_{p_i}$  and  $\vec{P}_{p_i}$  ( $i = 1, 2$ ) are the total energies and momenta of the two outgoing protons registered in coincidence. Fig. 3 presents the missing mass spectrum, built for all pairs of coincident protons registered in FD. Similar histogram has been built for breakup events generated with Monte Carlo simulation. Since all the cuts applied in analysis procedures are the same for experimental and simulated data, the model of hadronic interactions applied in simulation can be verified by comparing the missing mass spectra. This check is in turn important for effi-

ciency corrections. The qualitative agreement of shapes can be observed, while the remaining differences can be attributed to background of accidental coincidences and influence of electronic thresholds on the data, both mechanisms absent in the simulation. The missing mass histograms for data and MC will be further discussed, also quantitatively, in sec. II B 5.

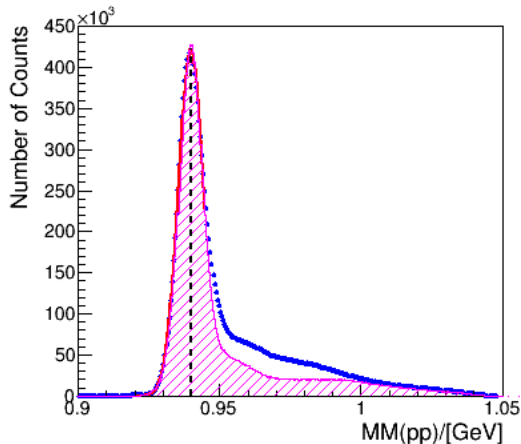


FIG. 3. (Color online) Missing mass reconstructed from momenta of two outgoing protons detected in coincidence (full points). Clearly, the peak corresponding to the neutron mass dominates. Red line represents Gaussian fit with mean value of 0.94 GeV. The right tail of the distribution originates from proton energy loss due to hadronic interactions and from accidental coincidences. The data are compared to histogram built on the basis of MC simulation (hatched magenta histogram).

After the selection of proton-proton coincidences and having performed the energy calibration, any kinematical configuration of the breakup reaction within the angular acceptance of the detection system can be analysed. The configuration has been defined by emission angles of the two outgoing protons: two polar angles  $\theta_1$  and  $\theta_2$  and their relative azimuthal angle  $\varphi_{12}$ . The data are integrated over the angular ranges of  $\theta_{1,2}$  ( $\pm 1^\circ$ ) and  $\varphi_{12}$  ( $\pm 5^\circ$ ). These ranges are large as compared to angular resolution of the detectors and, therefore, no significant systematic uncertainty is related to the determination of solid angles obtained for selected configurations. The effect of averaging of cross section within the angular ranges is taken into account when comparing the data with the theoretical calculations, which have been averaged accordingly and projected onto relativistic kinematics [19]

The sample kinematical spectrum  $E_1$  versus  $E_2$  obtained for selected configuration is shown in Fig. 4, top panel. The center of the band formed by experimental data is lying on the relativistic kinematics curve (corresponding to the point-like, central geometry). Correct kinematic relations of the data confirm accuracy of the energy calibration. In the next step, new variables are introduced:  $D$  is the distance of the  $(E_1, E_2)$  point from

the kinematic curve in the  $E_1$ - $E_2$  plane and  $S$  denotes the value of the arclength along the kinematical line with the starting point ( $S=0$ ) chosen arbitrarily at the point where  $E_2=0$  and starts to rise. The events contained within the distance  $D$  of  $\pm 20$  MeV from the kinematical line are selected for further analysis and presented in  $S$  vs.  $D$  spectrum (see Fig. 4, bottom panel).

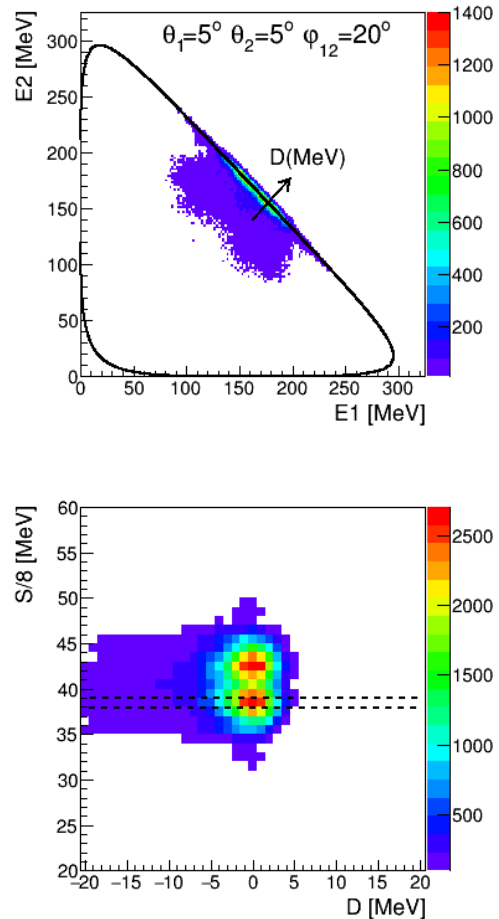


FIG. 4. (Color online) *Top panel* :  $E_1$  vs.  $E_2$  coincidence spectrum of the two protons registered at  $\theta_1=5^\circ \pm 1^\circ$ ,  $\theta_2=5^\circ \pm 1^\circ$ , and  $\varphi_{12}=20^\circ \pm 5^\circ$ . The solid line shows a three-body kinematical curve, calculated for the central values of experimental angular ranges.  $D$  axis illustrates the distance of the  $(E_1, E_2)$  point from the kinematical curve. *Bottom panel*: transformation of  $E_1$  vs.  $E_2$  spectrum to  $S$  (arclength) vs.  $D$  (distance from kinematical line in  $E_1$ - $E_2$  plane). Dashed lines represent integration limits ( $\Delta S=8$  MeV) for a sample  $S$ -slice.

The procedure of background subtraction is presented in Fig. 5. Each slice on the  $S$  vs.  $D$  spectrum (see Fig. 4, bottom panel) is treated separately. The background is approximated by a linear function between the two limits of integration ( $D_a, D_b$ ) defined as  $-3\sigma$  and  $+3\sigma$  from the peak position (Fig. 5, top panel). The  $D$ -projected distributions obtained after the background subtraction have Gaussian shape (with exception of bins

characterised by low signal-to-background ratio, see discussion in Sec. II B 6). The Gaussian distribution is fitted in the range from  $D_a$  to  $D_b$  (see Fig. 5, bottom panel). Number of events obtained after background subtraction is presented as a function of the arclength  $S$ , see an example in Fig. 6. After normalization to the integrated luminosity, the differential cross section is obtained.

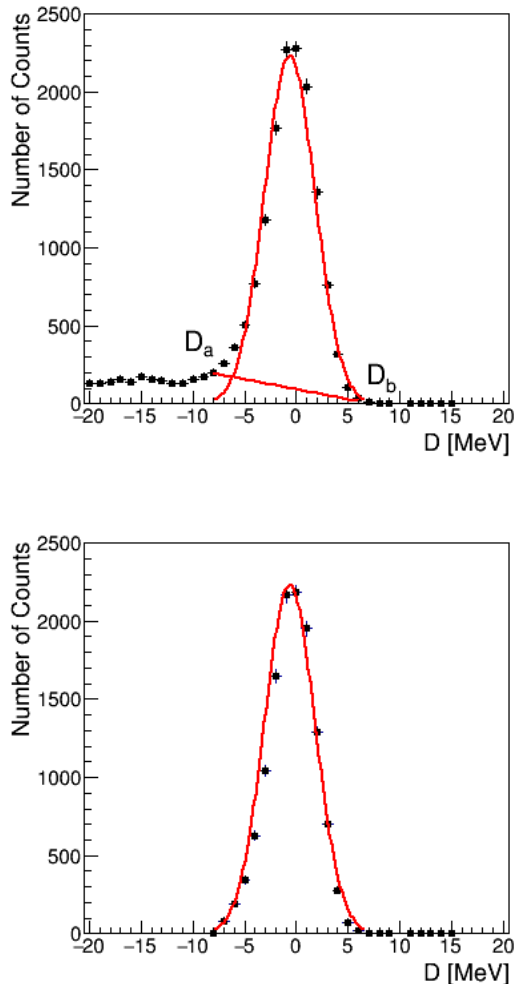


FIG. 5. (Color online) *Top panel*: Determination of the background contribution in one slice in the  $S$  vs.  $D$  spectrum (Fig. 4, bottom panel). The background is estimated by a linear function between limits of integration ( $D_a$ ,  $D_b$ ) (shown with the solid red line). *Bottom panel*:  $D$ -projected distribution after the background subtraction with a Gaussian distribution fitted in the range of  $D$  corresponding to distance of  $-3\sigma$  and  $+3\sigma$  from the peak center.

#### 4. Cross section normalization

For the purpose of normalization of the experimental results, the luminosity is determined on the basis of the number of the elastically-scattered deuterons.

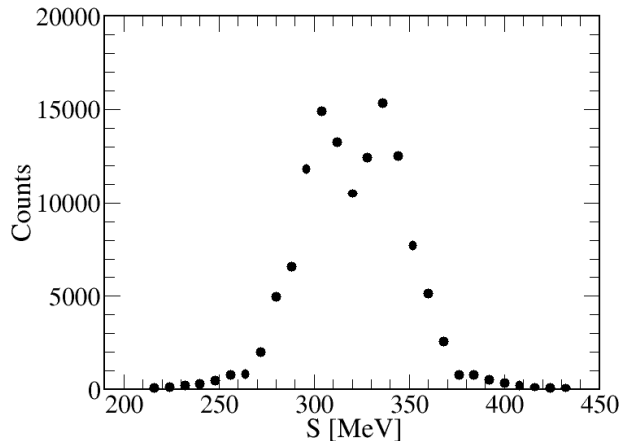


FIG. 6. An example of  $S$  distribution of the rate of breakup events obtained for the chosen kinematical configuration ( $\theta_1=5^\circ\pm 1^\circ$ ,  $\theta_2=5^\circ\pm 1^\circ$ , and  $\varphi_{12}=20^\circ\pm 5^\circ$ ). Statistical errors are smaller than the point size.

Selection of deuterons registered in the FD has been based on the  $\Delta E$ - $E_R$  technique. After applying energy calibration for protons the energy calibration for deuterons has been readjusted with the use of MC simulation. Kinematics of deuterons registered in FD obtained after the corrections is shown in Fig. 7. Particles which have not reached the 3rd FRH layer are not accepted.

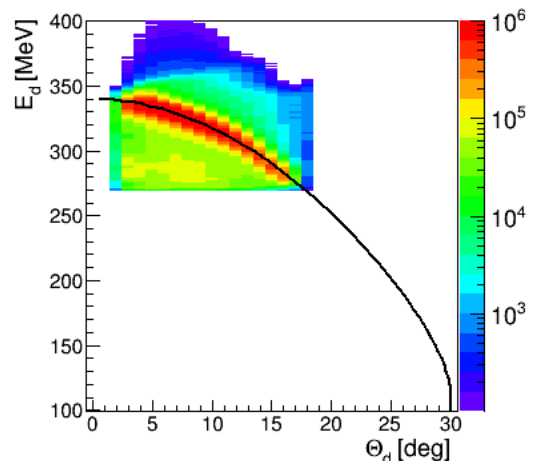


FIG. 7. (Color online) The energy vs.  $\theta_d$  polar scattering angle distribution for events identified as deuterons. Solid curve corresponds to kinematics of elastically scattered deuterons.

In order to obtain the luminosity a reference cross section  $\sigma_{LAB}^{el}$  for elastic scattering at the studied energy should be known at angle contained within the acceptance of our detector. It is the case, although the  $^2\text{H}(p, dp)$  cross section distribution measured at 170 MeV reveals irregularities which suggest systematic errors, see Fig. 8. It is extremely difficult to control the absolute



cross section value with an accuracy of 5%: The comparison of experimental data with theoretical calculation including the 3NF, [38–42] has shown not only rising with energy deficiency of calculations at the cross section minimum, but also scatter of the data exceeding their statistical errors [43]. In order to minimize the bias of the results, the normalization is based on all the data sets from the range of energies (between 108 and 200 MeV) compared to theoretical predictions. Deuterons scattered at angles covered by FD correspond to  $\theta_{CM}^p < 50^\circ$ , where the theoretical calculations including 3NF provide precise description of the data, see Fig. 9. On the basis of the available data, the dependence of cross section on beam energy can be studied at each polar angle, see examples in Fig. 10. Theoretical calculations including TM99 3NF (full points, solid lines) provide consistent description of the data, with exception of the lowest studied angle of  $8^\circ$  in the laboratory system. Trends of experimental data (polynomials presented as dashed lines) are based on all the data points (squares) but the one measured at 170 MeV (triangle). Finally, we applied three ways to obtain luminosity: taking values of the cross section  $\sigma_{LAB}^{el}(\theta_d)$  given by (a) calculations, (b) measurement at 170 MeV, and (c) the polynomial fit to other data sets. In each case the following formula is used to obtain the luminosity integrated over the measurement time:

$$L = \frac{N_{el}(\theta_d)}{\sigma_{LAB}^{el}(\theta_d) \Delta\Omega_d \epsilon^{el}(\theta_d)}, \quad (2)$$

where  $N_{el}$  is a number of elastically scattered deuterons registered at the deuteron emission angle  $\theta_d$  (during the certain time),  $\Delta\Omega_d$  is the solid angle for registering deuterons and  $\epsilon^{el}(\theta_d)$  is a detection efficiency for deuterons determined with the use of MC simulation. In order to control the result, the procedure is repeated for each deuteron polar angle between  $8^\circ$  and  $14^\circ$ , see Fig. 11. The spread of luminosity values obtained at the lowest deuteron polar angle of  $8^\circ$  is large, as expected from the above discussion. At the largest angles,  $13^\circ$  and  $14^\circ$ , significant systematic uncertainty is related to proton background leaking through the deuteron gate. The contribution of this background is estimated on the basis of MC simulation. Conservatively, the largest error due to neglecting this contribution is taken as the systematic uncertainty. The ranges of luminosity values obtained at all studied angles are consistent with each other. The final result has been obtained neglecting points at marginal angles of 8 and 14 degrees, due to their large systematic errors. Finally, the average integrated luminosity obtained for the full set of data is  $(2.437 \pm 0.005) \cdot 10^7 \text{ mb}^{-1}$  with systematic error of -2%, +3%. It is presented in Fig. 11 as a solid horizontal line with error limits shown as dashed lines.

The differential breakup cross section for a chosen angular configuration normalized to integrated luminosity value is given by the following formula:

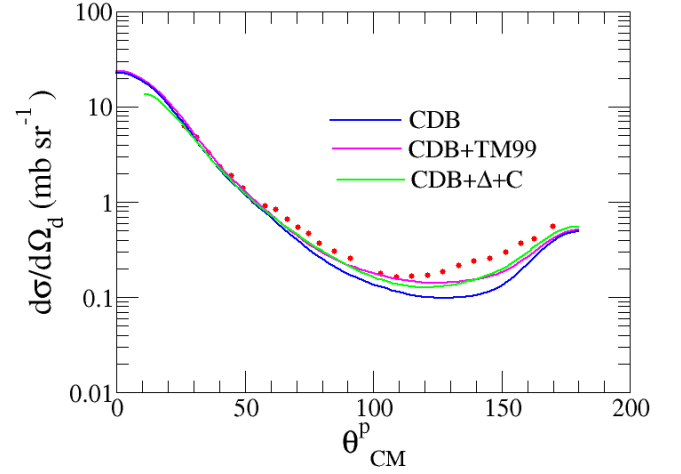


FIG. 8. (Color online) Angular distribution of the elastic scattering cross section in the CM system. Red dots represent the measured cross-section values for elastic scattering at  $E_p=170$  MeV [38]. The solid lines show the results of the theoretical calculations with the CD Bonn potential and the TM99 3NF as well as coupled-channel potential CD Bonn+ $\Delta$  and Coulomb force included (CDB+ $\Delta$ +C).

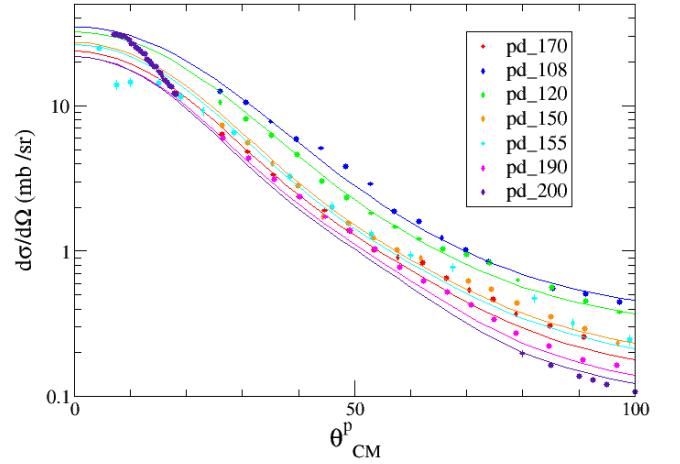


FIG. 9. (Color online) Experimental differential cross section of the reaction  $^2\text{H}(p, dp)$  in the CM system in the angular range of FD, at the incident-beam energies: 108 MeV, 120 MeV, 150 MeV, 170 MeV, 190 MeV [38] and 155 MeV [39], 200 MeV [41, 42]. The solid lines show the results of the theoretical calculations with the CD Bonn potential and the TM99 3NF.

$$\frac{d^5\sigma(S, \Omega_1, \Omega_2)}{d\Omega_1 d\Omega_2 dS} = \frac{N_{br}(S, \Omega_1, \Omega_2)}{L \Delta\Omega_1 \Delta\Omega_2 \Delta S \epsilon^{br}(S, \Omega_1, \Omega_2)}, \quad (3)$$

where  $N_{br}$  is the number of breakup coincidences registered at the angles  $\Omega_1, \Omega_2$  and projected onto a  $\Delta S$ -wide arclength bin. Subscripts 1 and 2 refer to two protons registered in coincidence. Numbering of protons is defined by condition:  $\theta_1 \leq \theta_2$  (for equal angles numbering is

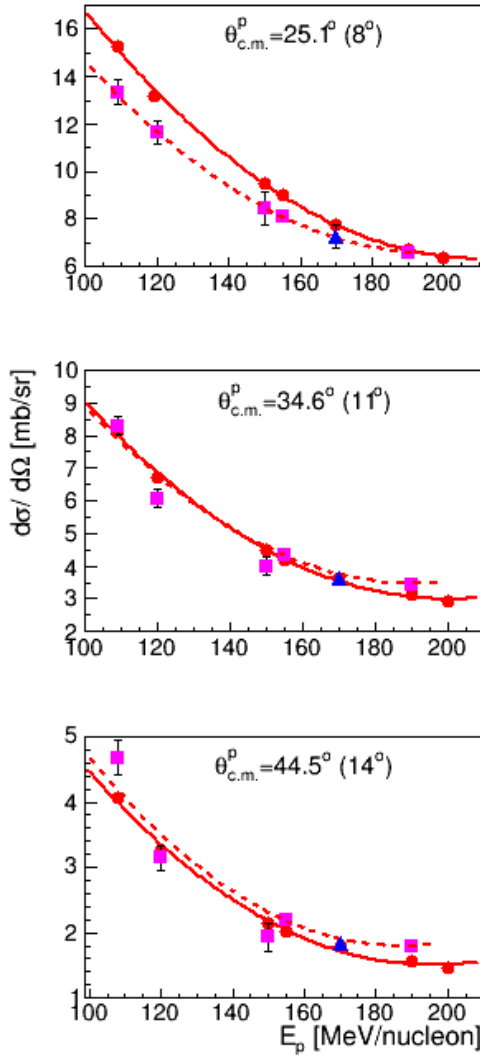


FIG. 10. (Color online) Experimental (triangles, squares and dashed lines) and theoretical (full points and solid lines) cross section for elastic scattering at given  $\theta_{c.m.}$  angle (corresponding  $\theta_{lab}$  in the bracket) presented in function of incident beam energy per nucleon. Dashed lines represent polynomial fitted to experimental points (excluding the point at 170 MeV). The solid lines present fitted functions to points obtained from theoretical calculations.

randomized).  $\Delta\Omega_i$ , with  $i=1, 2$ , denotes the solid angles ( $\Delta\Omega_i = \Delta\theta_i \Delta\varphi_i \sin\theta_i$ ) and  $\epsilon^{br}(S, \Omega_1, \Omega_2)$  is a product of all relevant efficiencies determined for each angular configuration. The normalization of the breakup cross section to the known cross section for elastic scattering, see Eq. (2), has the important advantage: electronic dead-time, trigger efficiency, the charge collected in Faraday Cup, the number of beam particles passing through the pellet target, etc. affect in the same way  $N_{br}$  and  $N_{el}$  and cancel in the ratio.

WASA Monte Carlo program was used for precise determination of efficiency of the detection system ( $\epsilon$ ). Including detector acceptance and all cuts applied in the

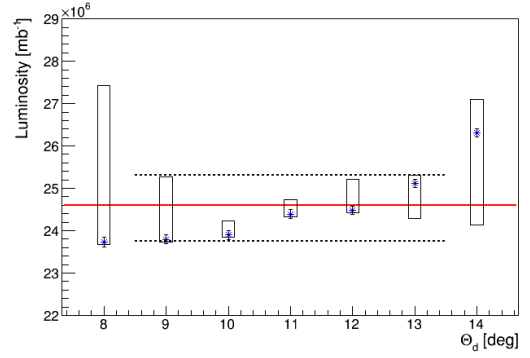


FIG. 11. (Color online) Determination of the integrated luminosity. The values of the luminosity are presented as a function of the deuteron scattering polar angle. The stars show results obtained with method (c). The solid line corresponds to the weighted average of five results with the smallest systematic errors (shown as boxes). The dashed lines represent the range of systematic error of the averaged luminosity (2%-3%).

analysis, detector efficiency for registering and identifying elastically scattered deuterons is about 80%. The efficiency of the detection system for proton-proton coincidences obtained for each kinematical configuration with defined integration limits:  $\Delta\theta_1=\Delta\theta_2=2^\circ$  and  $\Delta\varphi_{12}=10^\circ$  is presented in Fig. 12. The pits in the distributions reveal clear angular pattern, since they are caused by loss of events when both protons hit the same detector element. Due to low efficiency and possible inaccuracies related to the limit of the detection acceptance, configurations with  $\theta_{1,2}=17^\circ$  were not included into analysis.

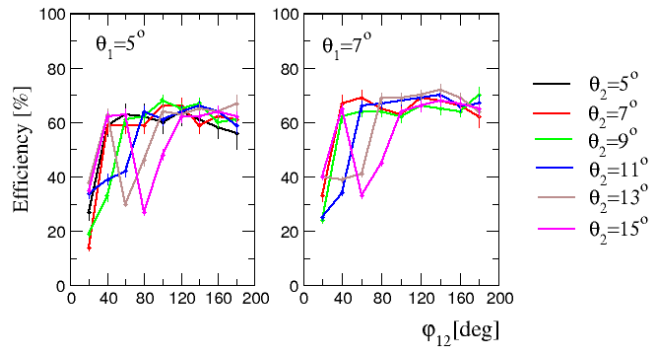


FIG. 12. (Color online) Efficiency of the detection of proton-proton coincidences determined on the basis of MC simulation. The results for a number of selected kinematical configurations ( $\theta_1, \theta_2, \varphi_{12}$ ) are shown as points with statistical errors. Lines are added to guide the eye.

### 5. Data consistency checks

The core analysis has been performed on the basis of the data collected with the main trigger in FD (trig-



ger No. 7, see Sec. II A). In order to check consistency and stability of the result, the luminosity is determined for three different data sets (of equal size) under condition of trigger No. 7 and for one of these data sets under condition of much less restrictive trigger No. 2. The results (Fig. 13) confirm stability of the obtained integrated luminosity values with the same trigger, while the difference between values of luminosity obtained for data collected with two trigger types is about 8%. This might suggest different background contribution to the events registered with these two triggers. However, it has been checked that for both triggers the background contribution is very similar, of about 13%-15% (at angles  $\theta_d < 13^\circ$ , where contribution of proton background is negligible). On the other hand, the same ratio of rates is obtained for the breakup data collected with those triggers. Therefore, we can interpret the difference as a loss of events due to the restrictive trigger condition, i.e. as an efficiency of the trigger. In the next step the influence of the trigger on final results for the breakup data is checked (see Fig. 14). There is no statistically significant difference, which indicates that the elastic scattering and breakup data are affected by the trigger efficiency in a similar way, which leads to cancellation of the effect in the ratio (Eq. 3).

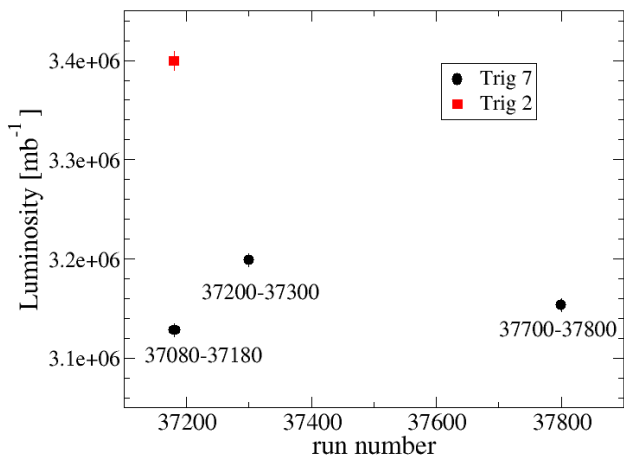


FIG. 13. (Color online) Comparison of the luminosity values obtained on the basis of data collected with different trigger and/or different time of the data collection (different ranges of the run numbers, as shown in the Figure). Statistical errors are smaller than the point size.

It has been observed that data reveal systematically the wider  $S$  distributions than all the theoretical predictions (see example in Table III), even in spite of the fact that averaging over the angular ranges has been applied to the theoretical calculations. Nevertheless, the impact of averaging on the width of the distributions has been studied both in the data and calculations. The comparison of FWHM's shown in Table III leads to the conclusion that the difference cannot be explained by effects of averaging. Procedure of projecting theoretical calculations onto the relativistic kinematics does not change

TABLE III. Full Width at Half Maximum for distributions presented in Fig. 14

distributions	Trigger	$\Delta\theta_1, \Delta\theta_2, \Delta\varphi_{12}$	FWHM $\pm\Delta$ FWHM
data	7	$2^\circ, 2^\circ, 10^\circ$	$60.0 \pm 8.2$
data	7	$1^\circ, 1^\circ, 5^\circ$	$61.3 \pm 8.1$
data	2	$2^\circ, 2^\circ, 10^\circ$	$59.6 \pm 8.3$
CDB+ $\Delta$ +C	-	$2^\circ, 2^\circ, 10^\circ$	56.3
CDB+ $\Delta$ +C	-	only central values	55.4

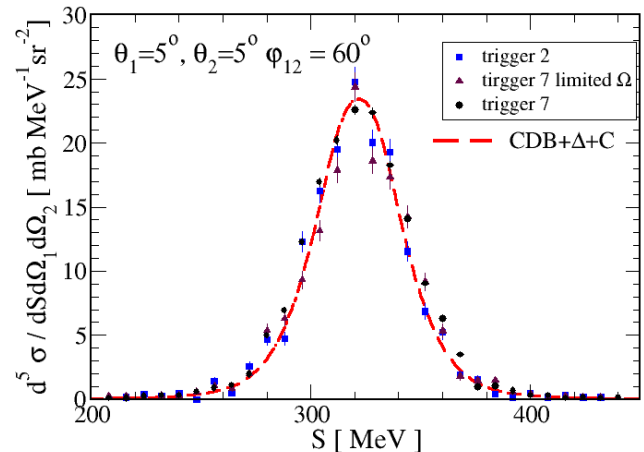


FIG. 14. (Color online) Example of the differential cross section of the breakup reaction as a function of the  $S$  value obtained at different conditions: with triggers 2, 7 and with trigger 7 combined with narrower limits on the solid angle. The calculation within the coupled-channel potential CD Bonn+ $\Delta$  and the Coulomb force included is represented by a red dashed line. Full Widths at Half Maximum (FWHM) of the presented distributions are collected in Table III.

the width of the resulting distribution, either. In Fig. 14 the cross section obtained with a limited solid angle (the event integration ranges) of  $\Delta\theta_1=\Delta\theta_2=1^\circ$  and  $\Delta\varphi_{12}=5^\circ$  is compared to the one obtained in the standard analysis. There is no significant change in shape or height of the distributions. The sums of data points (integrated distributions) are also equal within the limits of their statistical uncertainties.

The efficiency corrections, discussed in sec. II B 5, rely on simulations of particle interactions in the WASA detection system. Since hadronic interactions reduce registered energy of particles, the neutron mass reconstructed from momenta of two protons is distorted. Therefore the missing mass spectra are used to control this effect in the data and the MC simulations. The spectra presented in Fig. 3 have been integrated in the region of  $\pm 3$  sigma around the neutron peak ( $N_{peak}$ ) and in the whole range ( $N_{all}$ ) in order to compare the contribution of distorted events in the experimental and simulated data. The correction for the distorted events,  $N_{all}/N_{peak}$  ratio, is 1.47 in experiment and 1.31 in MC simulations. The

experimental data show relatively 12% larger effect, but the difference can be partially attributed to contribution of accidental coincidences. From estimates of this contribution and taking into account partial cancellation of the hadronic effect in detection efficiency for deuterons and proton pairs (Eq. 1), systematic error of 7% is attributed to possible underestimated hadronic interactions in Geant 3 simulation.

### 6. Experimental uncertainties

Statistical errors of the measured cross-section values comprise an uncertainty of the measured number of the breakup coincidences and of the luminosity. In all 189 kinematic configurations the statistical error in maximum of the cross-section distribution is 2% or less.

The systematic error of the cross-section stems primarily from three sources: detection efficiency, luminosity determination and background subtraction procedure. Uncertainty of determination of efficiency for proton-proton coincidences corresponds to statistical accuracy of MC simulation and varies between 1% and 4%, reaching up to 7% for configurations with the lowest  $\varphi_{12}=20^\circ$  values (see Fig. 12). Typical uncertainty of the background subtraction is of about 5%. Only at low cross section values, mainly at the tails of the studied  $S$ -distributions, signal-to-background ratio reaches low values of 6 and the background subtraction introduces significant uncertainty of 13%. Systematic uncertainty of the luminosity is between -2% and 3%. Finally, systematic uncertainties of data points vary between 6% and 18%, dominating the total uncertainty of the result. They are presented as bands on the  $S$  distributions (Figs. 17 - 19) and included into calculations of  $\chi^2$ .

## III. THEORETICAL CALCULATIONS

Theoretical calculations for the systems of three nucleons are performed using exact nonrelativistic three-body theory. The system of coupled equations for transition operators, proposed by Faddeev [44] or Alt, Grassberger and Sandhas (AGS) [45], are solved in momentum space. The models of nuclear interactions are the input to these calculations. Generally, the nuclear interactions applied to these calculations are constructed in one of three different ways described below.

In the first approach, semi-phenomenological models of nucleon-nucleon interaction are used, which base on the meson-exchange theory and have also a phenomenological part describing a short-range interaction with parameters fitted to the two-nucleon data. There exist several so-called realistic NN potential models based on this approach, like charge dependent (CD) Bonn [1], Argonne  $V_{18}$  [2] and Nijmegen I and II [3], providing an excellent description of two-nucleon observables. These potentials can be combined with models of three-nucleon

force. The state-of-the-art 3NF's are refined versions of the Fujita-Miyazawa force [46], in which one of the nucleons is excited into intermediate  $\Delta$  via  $2\pi$ -exchange with both nucleons. In the general case a pion emitted by one nucleon interacts with a second nucleon and then is absorbed by a third nucleon. The modern version of the  $2\pi$ -exchange Tucson-Melbourne (TM) 3NF model [47–49], called TM99 3NF, is consistent with chiral symmetry [7]. It contains only one cut-off parameter,  $\Lambda_{TM}$ . The value of  $\Lambda_{TM}$  is adjusted to reproduce the value of the  $^3H$  binding energy [52]. When the 3N system dynamics is studied with the AV18 NN potential also the Urbana IX 3NF [8] can be used. This force contains the two-pion exchange contribution due to intermediate  $\Delta$  excitation supplemented by a purely phenomenological repulsive short-range part.

The other approach extends the nucleon-nucleon interaction picture to non-nucleonic degrees of freedom within the Coupled-Channels Potential (CCP). It is based on the realistic CD Bonn potential, but extended to include the  $\Delta$ -isobar as an active degree of freedom [50, 51]. In the energy range below the pion-production threshold, where the  $\Delta$ -isobar excitation is virtual, it is assumed to be a stable baryon with real mass of 1232 MeV. The CCP is based on the exchange of  $\pi$ ,  $\rho$ ,  $\omega$ ,  $\sigma$  mesons, with contribution of the transition between the NN and  $N\Delta$  states, as well as the exchange  $N\Delta$ - $\Delta N$  potential. For the 3N system virtual excitation of  $\Delta$ -isobar yields an effective 3NF. There is also a contribution to the transition amplitude of the so-called two-baryon dispersion in NN system. These two contributions usually compete, therefore the net effects of including  $\Delta$ -isobar are suppressed as compared to the effects of the model 3NFs.

The most extensive developments of nuclear potentials are nowadays carried out within the framework of the Chiral Perturbation Theory (ChPT). This effective field theory bases on the most general Lagrangian for Goldstone bosons (pions) and matter fields (nucleons) consistent with the broken chiral symmetry of the QCD [4, 6]. Resulting interaction consists of long range and medium range pions exchanges, and contact interaction, with the associated low energy constants. In the framework of ChPT the nuclear potential is obtained in a way of a systematic expansion in terms of momentum variable:  $(Q/\Lambda)^\nu$ , where  $Q$  refers to a momentum of the nucleons,  $\Lambda$  is connected to the chiral symmetry breaking scale and  $\nu$  encounters expansion order. One of the most important features of the ChPT is the possibility to derive consistent many-body forces on the top of two-body ones. The first non-vanishing 3NF terms appear in the next-to-next-to-leading order (N<sup>2</sup>LO, 3rd order of chiral expansion,  $\nu=3$ ). Recently, the new version of chiral NN potential has been developed, with an improved semi-local regularization framework [53, 54]. In addition a new method of quantification of uncertainty due to the truncation of the chiral expansion has been proposed [55, 56]. The possibility of estimating the theoretical uncertainties of the obtained predictions is an exceptional advantage as

compared to other approaches, see also Ref. [57]. It has been shown, that with regard to NN interactions it is necessary to perform calculations at 5th order ( $\nu=5$ ), *i.e.* N4LO (see the discussion in [10]). Thus, the 3NF at the same order is required for the consistency. So far the complete calculations for Nd system at N3LO are unavailable. That is why only approaches based on the realistic potentials are considered in this work.

### A. Relativistic effects

Until recently, Faddeev calculations of observables in the deuteron breakup process were carried out in a non-relativistic framework. The relativistic treatment of the breakup reaction in 3N system is quite a new achievement [30, 31].

From the theoretical point of view, the dynamical relativistic effects taken into account are the boost of NN potential, relativistic deuteron wave function and form of Lippmann-Schwinger equation and proper treatment of Wigner rotations of spin states. Kinematical effects coming from relativistic phase-space factor are also included. The relativistic effects reveal at different parts of the breakup phase-space with various magnitude. The calculations for the  ${}^2H(n, nn)p$  breakup reaction showed that the relativistic effects tended to localize in phase-space regions characterized by small kinetic energy of the undetected proton and simultaneously the coplanarity of two neutrons ( $\varphi_{12} \approx 180^\circ$ ) [31]. The relativity can increase or decrease, depending on the phase-space region, the nonrelativistic cross section and magnitude of the effect increases with growing neutron energy. While at 65 MeV the influence of relativity effects is rather moderate ( $\sim 20\%$ ) at 200 MeV they can change the nonrelativistic cross section even by a factor of  $\sim 2$ .

### B. Coulomb interaction

With the aim to incorporate Coulomb interaction in calculations for proton-deuteron collisions, the Coulomb potential is screened and resulting scattering amplitudes are corrected by renormalization technique to match the unscreened limit. At first, the Coulomb interaction was applied to a purely nucleonic CDB potential and its coupled-channel extensions, CD Bonn+ $\Delta$  [25, 26]. In the next step, the Coulomb force was implemented in calculations with the realistic AV18 NN potential combined with the Urbana IX three-nucleon force [27]. In this way the Coulomb and 3NF effects can be studied not only separately but also together what allows us to understand their interplay in the deuteron-proton data.

## IV. RESULTS

The differential cross section for a regular grid of polar and azimuthal angles with a constant step in arclength variable  $S$  is obtained according to Eq. (3). Polar angles of the two protons  $\theta_1$  and  $\theta_2$  are changed between  $5^\circ$  and  $15^\circ$  with the step size of  $2^\circ$  and their relative azimuthal angle  $\varphi_{12}$  is analyzed in the range from  $20^\circ$  to  $180^\circ$ , with the step size of  $20^\circ$ . In total, 189 configurations have been analysed. For each combination of the central values  $\theta_1$ ,  $\theta_2$ , and  $\varphi_{12}$  the experimental data are integrated within the limits of  $\pm 1^\circ$  for the polar angles and of  $\pm 5^\circ$  for relative azimuthal angle. The bin size along the kinematic curve  $S$  is either 8 MeV or 24 MeV, depending on the data rate in this region, in order to obtain statistical uncertainty per data point below 2% in the maximum of the  $S$  distribution.

TABLE IV. Definition of abbreviations applied for naming theoretical calculations. “aver” means averaging over angular ranges accepted in data analysis.

abbreviation	description	aver	Ref.
2N	potentials: AV18, CD Bonn, Nijmegen I and II	Yes	[1]
			[2]
			[3]
2N+TM99	potentials (as above) with TM99 3NF	Yes	[47]
			[48]
			[49]
CDB	CD Bonn potential	Yes	[1]
CDB+ $\Delta$	coupled-channel potential CD Bonn+ $\Delta$	Yes	[50, 51]
CDB+ $\Delta$ +C	coupled-channel potential CDB+ $\Delta$ with Coulomb force	Yes	[25, 26]
CDBrel	CD Bonn potential relativistic calculations	No	[31]

The data are compared with the theoretical calculations listed in the Table IV. Prior to comparing with the data, a majority of the theoretical predictions has been averaged over the angular ranges accepted in the data analysis ( $\Delta\theta_{1,2} = 2^\circ$ ,  $\Delta\varphi_{12} = 10^\circ$ ) and projected onto relativistic kinematics, see Ref. [19]. Relativistic calculations are the only exception: the calculations are performed for central values of the angular ranges alone. The theoretical calculations using standard semi-phenomenological two-nucleon potentials, denoted in following NN, provide very similar results and are treated as a group: they are presented in figures as bands and, in calculations of  $\chi^2/\text{d.o.f.}$ , an average value of all predic-

tions is taken (corresponding to the middle of the band). Calculations using those potentials combined with the TM99 3NF (2N+TM99) are treated in an analogous way. The group of calculations, 2N, 2N+TM99, CDBrel, is performed with  $np$  interaction in 1S0 wave, while the second group, CDB, CDB+ $\Delta$  and CDB+ $\Delta$ +C, is performed using both  $pp$  and  $np$  interactions in all isospin triplet waves, including 1/2 and 3/2 total 3N isospin components.

Figs. 17 - 19 present examples of the differential cross section obtained for the chosen kinematic configurations of the breakup reaction (at the beam energy of 170 MeV/nucleon). Each of figures shows the set of experimental data compared to two different groups of theoretical calculations. In the top part the effects of 3NF (due to explicit treatment of  $\Delta$  isobar) and influence of Coulomb interaction are presented. In the bottom part the effects of TM99 3NF are shown. Fig. 17 presents configurations characterised with the lowest (among all analysed) proton polar angles ( $\theta_1 = \theta_2 = 5^\circ$ ), Fig. 19 - configurations with the largest proton polar angles ( $\theta_1 = \theta_2 = 15^\circ$ ), and Fig. 18 - sample configurations with asymmetric combination of proton polar angles ( $\theta_1=9^\circ$ ,  $\theta_2=13^\circ$ ). In the figures, the error bars represent the statistical uncertainties, often smaller than the data points. The systematic uncertainties are represented by hatched bands in the lower part of each individual panel. Full set of data has been presented in Ref. [58].

### A. $\chi^2$ analysis

Quantitative analysis of the description of the cross section data ( $\sigma_{exp}$ ) provided by various calculations ( $\sigma_{teor}$ ) is performed in terms of  $\chi^2$ -like variables. Due to dominating contribution of systematic uncertainties, the following definition has been applied:

$$\chi^2 = \frac{1}{n_{d.o.f.}} \sum \frac{(\sigma_{teor}(\xi) - \sigma_{exp}(\xi))^2}{(\Delta\sigma_{st}(\xi) + \Delta\sigma_{sys}(\xi))^2}, \quad (4)$$

where  $\xi$  represents a set of kinematic variables  $\xi=(\theta_1, \theta_2, \varphi_{12}, S)$ ,  $\Delta\sigma_{st}(\xi)$  and  $\Delta\sigma_{sys}(\xi)$  denote statistical and systematic uncertainties, respectively, summing goes over certain set of kinematic variables and  $n_{d.o.f.}$  is a number of data points included in this sum. So defined quantity has no precise statistical meaning, however, it is still a measure of description provided by different models. When its value reaches roughly 2 or more, it can be treated as a signal of inconsistency between the model predictions and the measured data.

The  $\chi^2$  per degree of freedom defined above is calculated globally, individually for the kinematic configurations and, in addition, for the data sorted according to combination of polar angles  $\theta_1, \theta_2$  and to relative azimuthal  $\phi_{12}$  of the two protons. Global analysis (see Fig. 15, left panel) shows the importance of Coulomb interaction in the studied region of phase space. Global

analysis indicates also certain improvement of description due to including of 3NF, both for TM99 force and in explicit  $\Delta$  isobar approach.

The analysis performed in function of  $\phi_{12}$  (see Fig. 15, right panel) indicates clearly the region of dominance of the Coulomb effect. As expected, the region of the lowest  $\phi_{12}$ , close to proton-proton FSI, is particularly sensitive to Coulomb interaction, which lowers cross section by a large factor (see also configuration  $\theta_1=5^\circ$ ,  $\theta_2=5^\circ$ ,  $\varphi_{12}=20^\circ$  in Fig. 17, top panel). The opposite influence of Coulomb interactions is present at the largest  $\phi_{12}$  (e.g. configuration  $\theta_1=5^\circ$ ,  $\theta_2=5^\circ$ ,  $\varphi_{12}=180^\circ$  in Fig. 17), which is also visible as an increase of  $\chi^2$  in Fig. 15, right panel. The region of intermediate angles of about  $60^\circ$ - $80^\circ$  is less sensitive to Coulomb repulsion between protons, though even there the effects are not negligible. In this region, the effect of 3NF shows up - not because of its particular strength, but since it is not covered that much by Coulomb effects. The improvement is similar in case of 2N+TM99 and CDBonn + $\Delta$  potentials.

The analysis of data sorted in function of combination of polar angles  $\theta_1, \theta_2$  (Fig. 16) provides another examples of the Coulomb force dominance in the FSI region, characterised by the lowest difference of polar angles.

Dominant influence of Coulomb interaction at forward proton emission angles (in laboratory system of the  $^1\text{H}(d, pp)n$  reaction) is in agreement with studies at other beam energies, see for example [24].

### B. Relativistic effects

Fig. 20 presents the set of configurations for which relativistic NN calculations have been performed. The result presented in the top left panel indicates an interplay of 3N interactions, Coulomb force and relativistic effects. For the configuration shown in the bottom panel all the calculations underestimate the experimental data. The discrepancy is even increased by relativistic calculations, which is also reflected in the  $\chi^2$  analysis.

## V. SUMMARY

The differential cross section of the  $^1\text{H}(d, pp)n$  reaction has been determined for the configurations characterised with forward proton emission angles in the laboratory system. In spite of the relatively high beam energy of 170 MeV/nucleon, the Coulomb interaction plays a dominant role in this region. The predicted 3NF effects are small or very moderate, nevertheless the description of the experimental data is improved by including the 3NF into calculations. It is observed in both approaches applied to modelling the 3N force and the improvement is seen in the region where the net Coulomb effects are moderate. None of the existing calculations, even the one including both

the Coulomb interaction and three- nucleon force, provides satisfactory description of the whole data set. The problem is observed at the largest studied polar angles of two protons:  $\theta_1, \theta_2 \geq 13^\circ$  combined with their large relative azimuthal angle  $\varphi_{12} > 120^\circ$ , where all the predictions underestimate the measured cross section. This effect can be associated with problem in describing the elastic scattering cross section at its minimum. On the other hand, the full relativistic treatment of the process is still missing. The relativistic calculations based on pure NN interaction show the effect opposite to the one needed for the correct data description, but it will be interesting to see contributions of 3NF included in relativistic calculations. The data set collected in the experiment under discussion contains also the strongly asymmetric configurations: coincidences with one proton registered in FD and the other one - in Central Detector (FD-CD), which correspond to the angular range  $5^\circ < \theta_1 < 15^\circ$ ,  $20^\circ < \theta_2 < 90^\circ$ . They will be used in forthcoming analysis to further explore the observed situation, along with the data collected at lower (170 MeV/nucleon) and higher

(190 and 200 MeV/nucleon) deuteron beam energies.

## ACKNOWLEDGMENTS

This work was partially supported by Polish National Science Center under Grants No. 2012/05/E/ST2/02313, No. 2012/05/B/ST2/02556 and No. 2016/22/M/ST2/00173. We thank the COSY crew for their work and the excellent conditions during the beam time.

- 
- [1] R. Machleidt, F. Sammarruca and Y. Song, Phys. Rev. C **53**, R1483 (1996);  
R. Machleidt, Phys. Rev. C **63**, 024001 (2001).
  - [2] R.B. Wiringa, V. G. J. Stoks and R. Schiavilla, Phys. Rev. C **51**, 38 (1995).
  - [3] V.G.J. Stoks, R.A.M. Klomp, C.P.F. Terheggen and J.J. de Swart, Phys. Rev. C **49**, 2950 (1994).
  - [4] P. F. Bedaque and U. van Kolck, Annu. Rev. Nucl. Part. Sci. **52**, 339 (2002).
  - [5] S. Weinberg, Phys. Lett. B **251**, 288292 (1990);  
S. Weinberg, Nucl. Phys. B **363**, 318 (1991).
  - [6] E. Epelbaum, H.-W. Hammer and U.-G. Meißner, Rev. Mod. Phys. **81**, 1773 (2009).
  - [7] S. A. Coon and H.K. Han, Few-Body Syst. **30**, 131 (2001).
  - [8] B.S. Pudliner, V.R. Pandharipande, J. Carlson, S.C. Pieper and R.B. Wiringa, Phys. Rev. C **56**, 1720 (1997).
  - [9] S. C. Pieper, V. R. Pandharipande, R. B. Wiringa and J. Carlson, Phys. Rev. C **64** 014001 (2001).
  - [10] R. Machleidt and F. Sammarruca, Phys. Scr. **91**, 083007 (2016).
  - [11] M. Viviani, Nucl. Phys. A **631**, 111c (1998).
  - [12] A. Nogga, H. Kamada and W. Glöckle, Phys. Rev. Lett. **85**, 944 (2000).
  - [13] S. C. Pieper and R. B. Wiringa, Ann. Rev. Nucl. Part. Sci. **51**, 53 (2001).
  - [14] P. Navrátil, V. G. Gueorguiev, J. P. Vary, W. E. Ormand, and A. Nogga, Phys. Rev. Lett. **99**, 042501 (2007).
  - [15] H. Witala, W. Glöckle, D. Hüber, J. Golak and H. Kamada, Phys. Rev. Lett. **81**, 1183 (1998).
  - [16] H. Hatanaka *et al.* Phys. Rev. C **66**, 044002 (2002).
  - [17] P. Mermod *et al.* Phys. Lett. B **597**, 243 (2004).
  - [18] N. Kalantar-Nayestanaki *et al.*, Rep. Prog. Phys. **75**, 016301 (2012).
  - [19] St. Kistryn, E. Stephan, J. Phys. G: Nucl. Part. Phys. **40**, 063101 (2013).
  - [20] A. Deltuva *et al.*, Phys. Rev. C **71**, 064003 (2005).
  - [21] H. Witala, J. Golak, W. Glöckle and H. Kamada, Phys. Rev. C **71**, 054001 (2005).
  - [22] St. Kistryn *et al.*, Phys. Rev. C **72**, 044006 (2005).
  - [23] St. Kistryn *et al.*, Phys. Lett. B **641**, 23 (2006).
  - [24] I. Ciepał *et al.*, Few-Body Syst. **56**, 665 (2015).
  - [25] A. Deltuva, A.C. Fonseca and P.U. Sauer, Phys. Rev. C **72**, 054004 (2005).
  - [26] A. Deltuva, A.C. Fonseca and P.U. Sauer, Phys. Rev. C **73**, 057001 (2006).
  - [27] A. Deltuva, Phys. Rev. C **80**, 064002 (2009).
  - [28] H. Mardanpour, "Investigation of nuclear forces in  $\vec{d} + p$  elastic and  $\vec{p} + d$  break-up reactions at intermediate energies", Phd Thesis, RUG, 2008.
  - [29] H. Mardanpour *et al.*, Few-Body Syst. **44**, 49 (2008).
  - [30] H. Witala *et al.*, Phys. Rev. C **83**, 044001 (2011).
  - [31] R. Skibiński, H. Witala and J. Golak, Eur. Phys. J. A **30**, 369 (2006).
  - [32] Ch. Bargholtz *et al.*, Nucl. Instrum. Methods Phys. Res., Sect. A **594**, 339-350 (2008).
  - [33] H. H. Adam *et al.*, arXiv:nucl-ex/0411038 (2004).
  - [34] Paweł Podkopał, "Investigations of the reaction  $dd \rightarrow {}^3\text{He} n \pi^0$  at 350 MeV beam energy with WASA-at-COSY", Phd Thesis, Cracow, Poland, 2011.
  - [35] U. Bechstedt *et al.*, Proceedings of the 1999 Particle Accelerator Conference, New York, 1701 (1999).
  - [36] H. Stockhorst *et al.*, Proc. of International Particle Accelerator Conference (IPAC), 23-28 May, Kyoto, Japan (2010).
  - [37] P. Vlasov, "Analysis of the  $\eta \rightarrow 3\pi^0$  decay in the pp interaction", Phd Thesis, Ruhr - Universität Bochum, Germany, 2008.
  - [38] K. Ermisch *et al.*, Phys. Rev. C **68**, 051001(R) (2003).
  - [39] K. Kuroda *et al.*, Phys. Lett. **13**, 67 (1964).
  - [40] K. Sekiguchi *et al.*, Phys. Rev. C **65**, 34003 (2004).
  - [41] R. E. Adelberger and C. N. Brown, Phys. Rev. D **5**, 2139

- (1972).
- [42] H. Rohdjeß *et al.*, Phys. Rev. C **57**, 2111 (1998).
  - [43] A. Ramazani Moghaddam Arani, “Cross section and analyzing power measurements in three and four-nucleon scattering”, Phd Thesis, RUG, 2009.
  - [44] L.D. Faddeev, Sov. Phys. JETP **12**, 1014 (1961).
  - [45] E.O. Alt, P. Grassberger and W. Sandhas, Nucl. Phys. B2, 167 (1967).
  - [46] J. Fujita and H. Miyazawa, Prog. Theor. Phys. **17**, 360 (1957).
  - [47] S. A. Coon *et al.*, Nucl. Phys. A **317**, 242 (1979).
  - [48] S. A. Coon and W. Glöckle, Phys. Rev. C **23**, 1790 (1981).
  - [49] W. Glöckle, S. A. Coon, Phys. Rev. C **23**, 1790 (1981).
  - [50] A. Deltuva, K. Chmielewski and P.U. Sauer, Phys. Rev. C **67**, 034001 (2003).
  - [51] A. Deltuva, R. Machleidt and P.U. Sauer, Phys. Rev. C **68**, 024005 (2003).
  - [52] A. Nogga, D. Hüber, H. Kamada and W. Glöckle, Phys. Lett. B **409**, 19 (1997).
  - [53] E. Epelbaum, H. Krebs and U.-G. Meißner, Eur. Phys. J. A **51**, 53 (2015).
  - [54] P. Reinert, H. Krebs and E. Epelbaum, Eur. Phys. J. A **54**, 86 (2018).
  - [55] E. Epelbaum, H. Krebs and U.-G. Meißner, Phys. Rev. Lett. **115**, 122301 (2015).
  - [56] S. Binder *et al.*, Phys. Rev. C **98**, 014002, (2018).
  - [57] R. Skibiński, Yu. Volkotrub, J. Golak, K. Topolnicki and H. Witała, Phys. Rev. C **98**, 014001, (2018).
  - [58] B. Kłos, “Studies of Relativistic Effects in the Deuteron-Proton Collisions”, Hab. Thesis of the University of Silesia, Katowice 2017 , ISBN 978-83-64804-65-6.



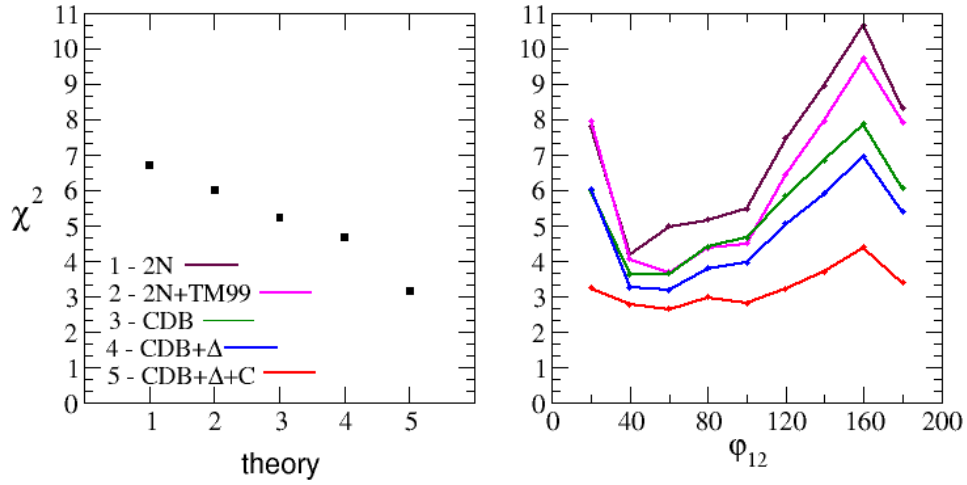


FIG. 15. (Color online) Quality of description of the differential cross section for the breakup reaction at 170 MeV/nucleon beam energy at forward angles. Left panel: The global  $\chi^2/d.o.f.$  obtained as a result of comparing the cross section data with each of five types of theoretical calculations specified in the legend. Right panel: The  $\chi^2/d.o.f.$  calculated for set of data characterised with given relative azimuthal angle  $\phi_{12}$

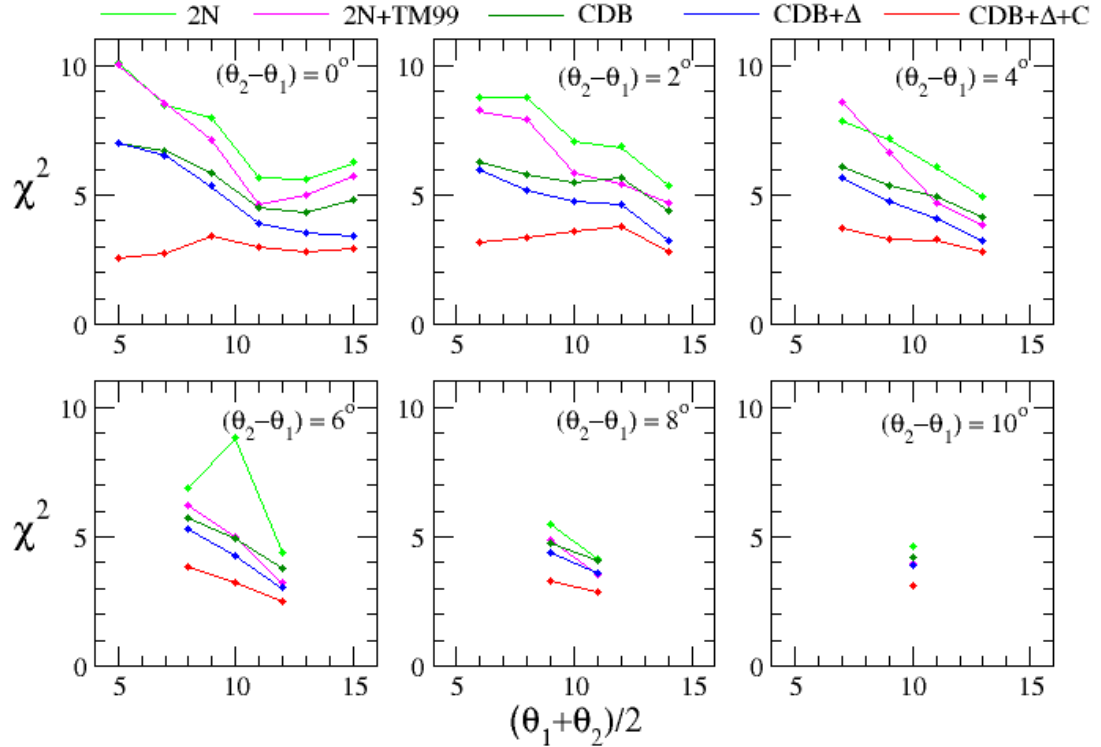


FIG. 16. (Color online) Similar to analysis shown in Fig. 15, right panel, but with  $\chi^2$  per degree of freedom calculated for each set of data characterised with the given combination of proton polar angles. The results are ordered according to difference of polar angles  $\theta_{12} = \theta_1 - \theta_2$ ; in each panel results for one value of  $\theta_{12}$  are shown.

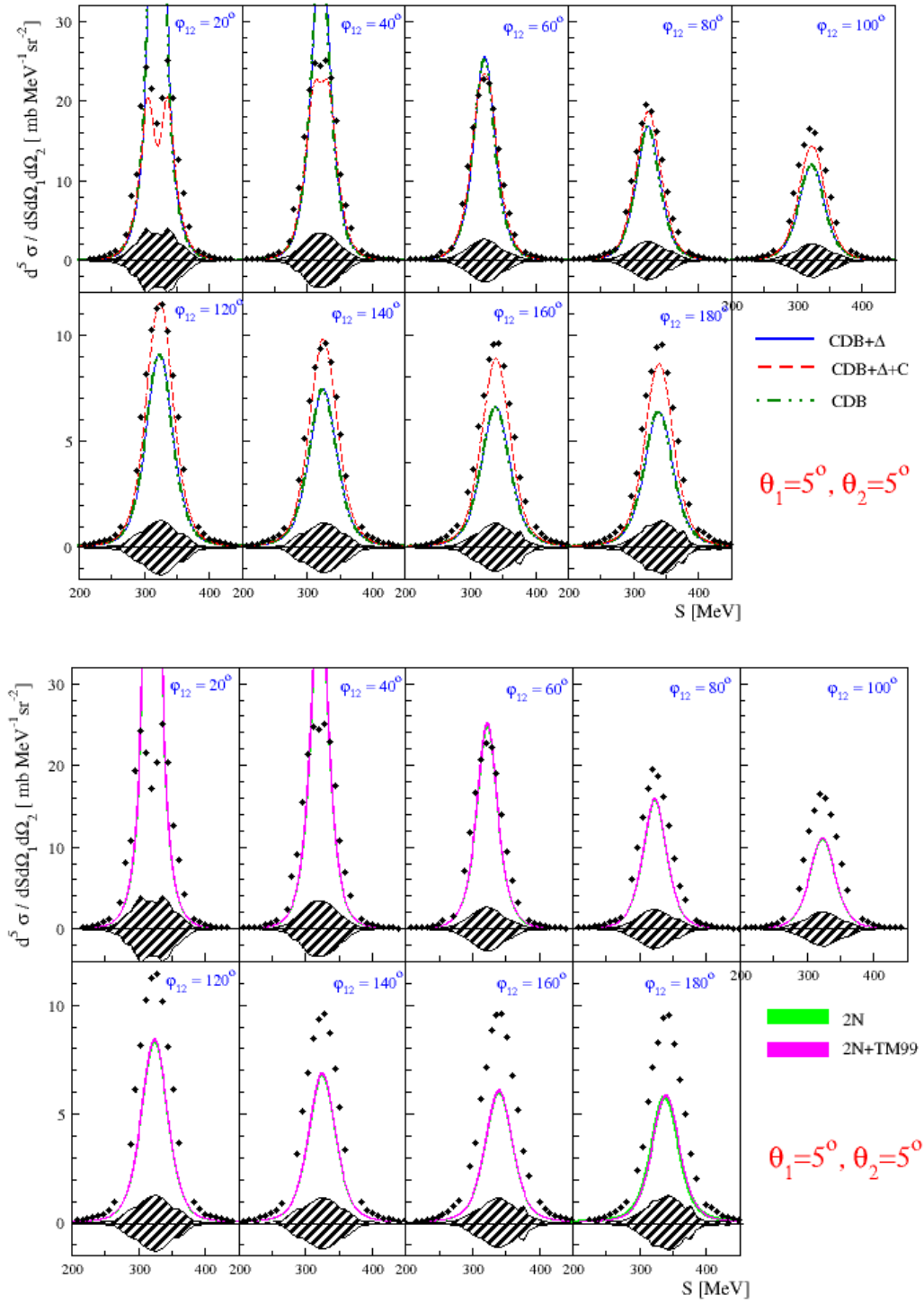


FIG. 17. (Color online) Differential cross section of  $^1\text{H}(d, pp)n$  breakup reaction at beam energy of 170 MeV/nucleon shown in function of  $S$  variable. The presented data belong to 9 kinematic configurations characterised with the same combinations of proton polar angles ( $\theta_1=5^\circ$ ,  $\theta_2=5^\circ$ ) and various relative azimuthal angles of the two protons, indicated in the individual panels. Statistical errors are smaller than the point size. Systematic uncertainties are represented by hatched band. **Top part:** data compared to predictions obtained for the calculations within the coupled-channel approach with the CD Bonn potential (CDB, dotted-dashed green line), with the CD Bonn +  $\Delta$  potential without (CDB+ $\Delta$ , blue solid line) and with the Coulomb force included (CDB+ $\Delta$ +C, red dashed line); **Bottom part:** the same data confronted with the predictions based on NN potentials: 2N (AV18, CD Bonn, Nijm I and II) (green band) and NN combined with the TM99 3NF (magenta band).

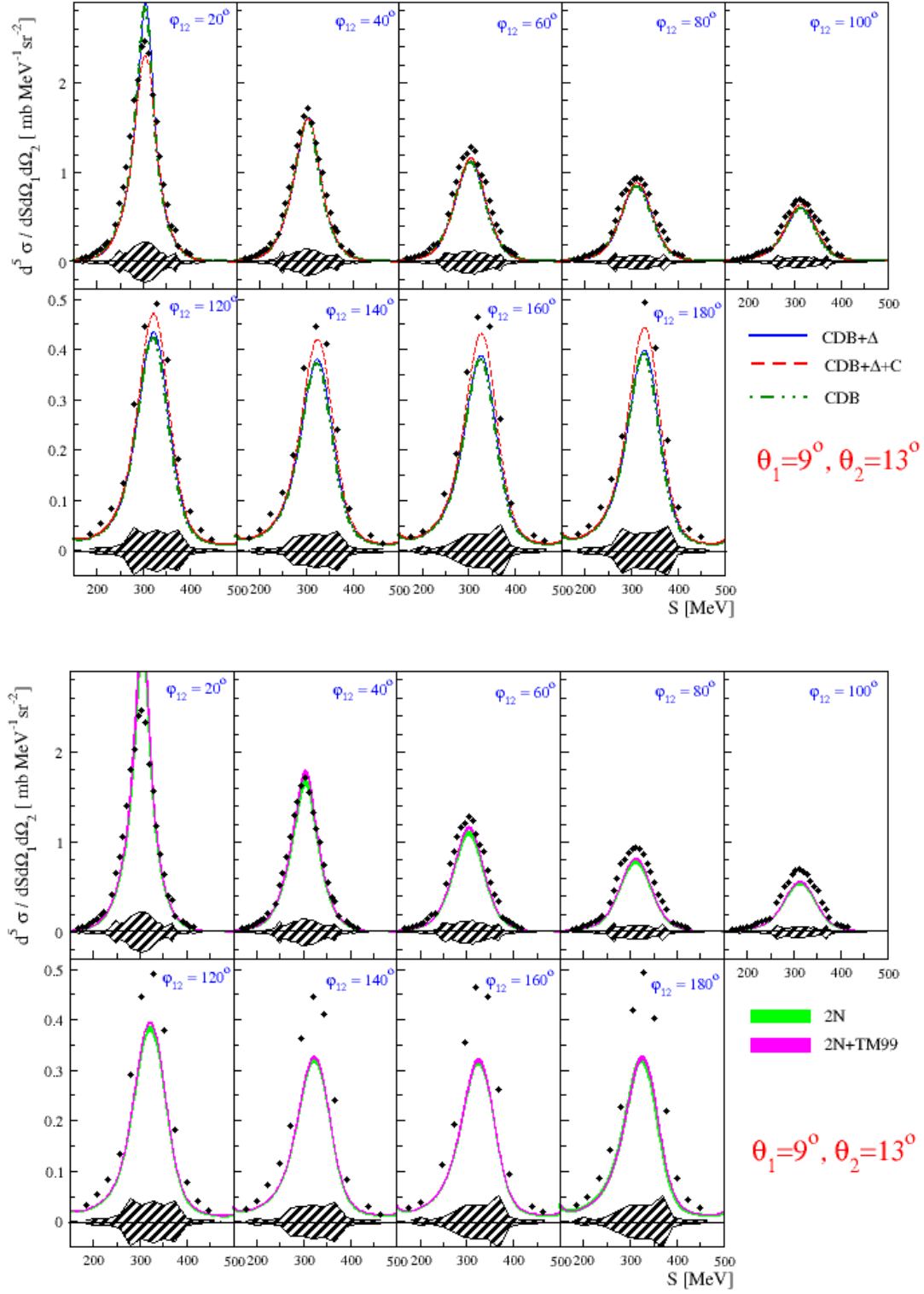


FIG. 18. (Color online) The same as Fig. 17 but for kinematic configurations with the proton polar angles  $\theta_1 = 9^\circ$ ,  $\theta_2 = 13^\circ$ .

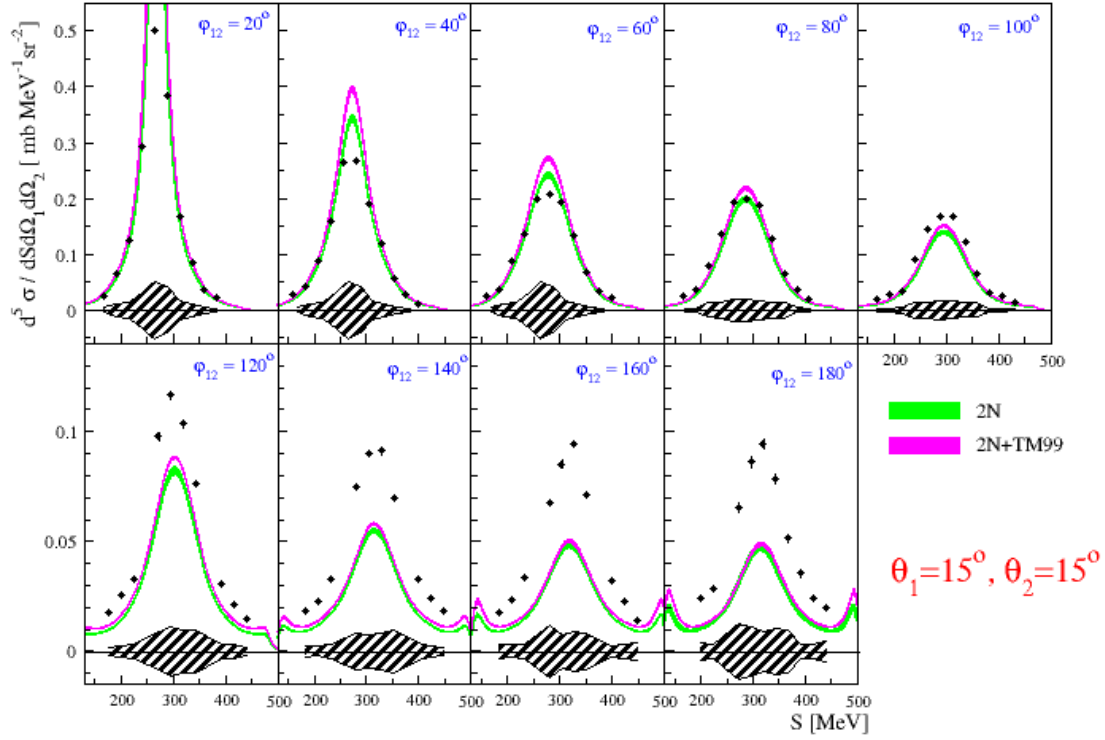
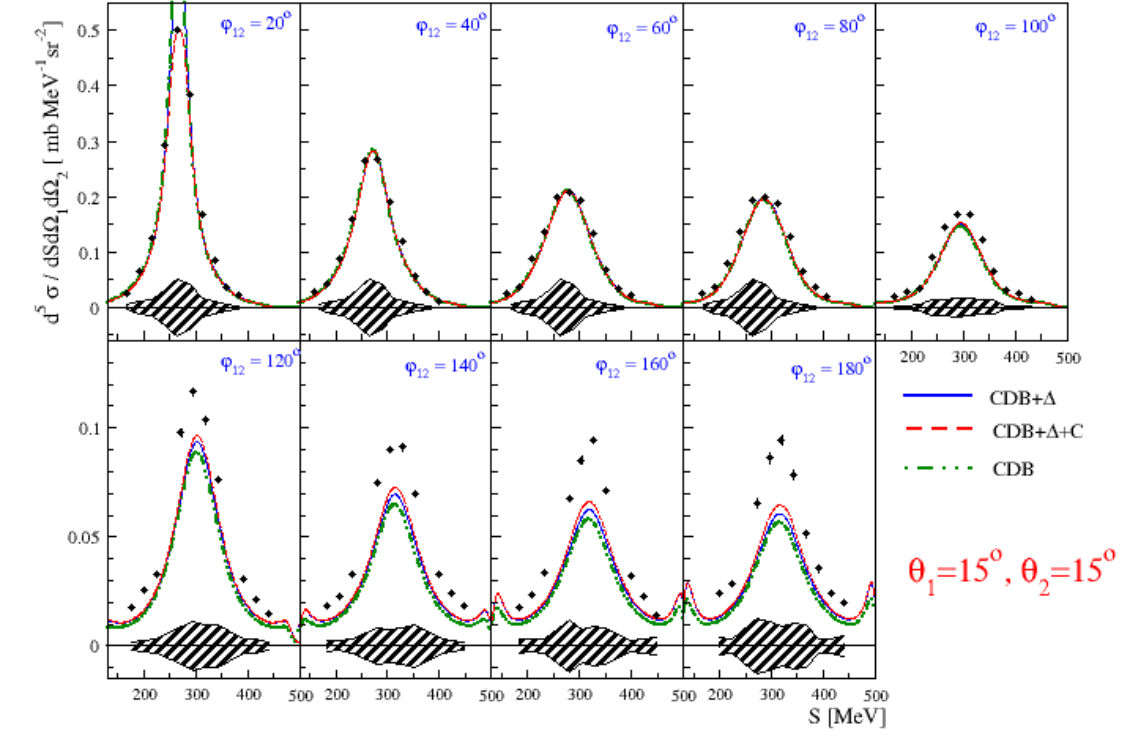


FIG. 19. (Color online) The same as Fig. 17 but for kinematic configurations with the proton polar angles  $\theta_1 = 15^\circ$ ,  $\theta_2 = 15^\circ$ .

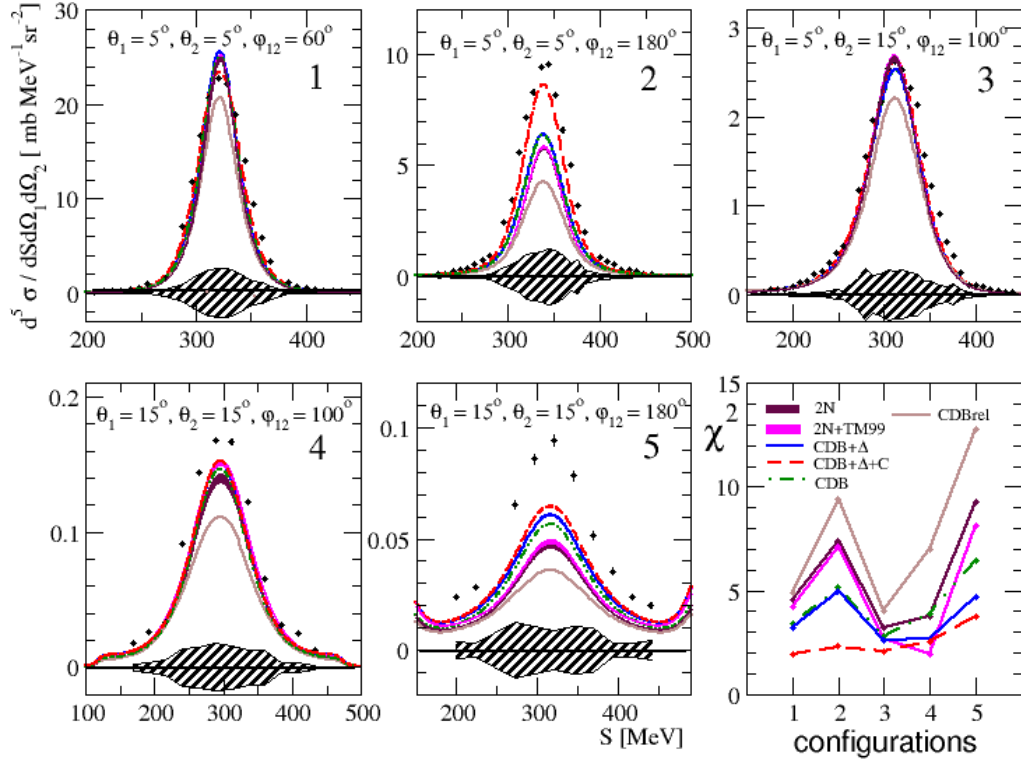


FIG. 20. (Color online) Similar to Fig. 17 but for the set of configurations for which relativistic NN calculations has been performed (shown as brown solid line). The bottom right panel shows the  $\chi^2/d.o.f.$  analysis performed for each configuration shown in this figure, numbered as in the panels. The brown points (connected by solid brown line) represent results of  $\chi^2/d.o.f.$  analysis with relativistic calculations.